Advanced Industrial and Engineering Polymer Research 8 (2025) 600–611

Contents lists available at ScienceDirect

Advanced Industrial and Engineering Polymer Research

journal homepage: http://www.keaipublishing.com/aiepr

Research paper

Ultra-expanded microcellular shape memory polymer foams via supercritical foaming for recyclable oil absorption and improved thermal insulation

Jialong Chai [a,b,c], Guilong Wang [a,b,*], Chao Wei [a,b], Xinyang Li [a,b], Runze Shao [a,b], Guoqun Zhao [a,b]

[a] State Key Laboratory of Advanced Equipment and Technology for Metal Forming, Shandong University, Jinan, Shandong 250061, China
[b] Key Laboratory for Liquid-Solid Structural Evolution and Processing of Materials (Ministry of Education), Shandong University, Jinan, Shandong 250061, China
[c] School of Fashion and Textiles, The Hong Kong Polytechnic University, Hung Hom, Kowloon, 999077, China

ARTICLE INFO

Article history:
Received 17 June 2025
Received in revised form
6 August 2025
Accepted 19 August 2025

Keywords:
Shape memory materials
Supercritical foaming
Fully miscible polymers
Oil absorption
Thermal insulation

ABSTRACT

Shape memory foams (SMFs) have garnered significant attention as smart, sustainable solutions for diverse applications, including environmental remediation and thermal insulation. However, their practical utility has often been constrained by limited expansion ratios resulted poor porosity, which hinder performance in key areas such as oil absorption and heat retention. In this study, we report the fabrication of ultralight SMFs based on the environmentally friendly supercritical foaming method. The exceptional miscibility of the polymer blends, validated by molecular dynamics analysis and thermo behaviors, enables the formation of foams with an extraordinarily high expansion ratio. This process yields microcellular structures with an ultralow density of 0.0265 g cm^{-3}, significantly enhancing both the porosity and surface area of the material. The high expansion ratio directly translates to superior oil absorption capacity, as the increased pore volume and interconnected microstructure facilitate rapid uptake and retention of oils. Simultaneously, the expanded cellular architecture imparts outstanding thermal insulation properties, effectively minimizing heat transfer and energy loss. The excellent shape memory behavior and recyclability, further underscoring their potential for sustainable applications. This research introduces a robust and eco-friendly strategy for producing high-performance SMFs with unprecedented expansion ratios, offering a versatile approach for environmental protection and energy conservation.

1. Introduction

In recent years, the development of shape memory foams (SMFs) has garnered significant attention, driven by the growing demand for sustainable, lightweight, and multifunctional materials across various industries [1–3]. SMFs exhibit the remarkable ability to recover their original shape when exposed to specific external stimuli, such as heat, light, or electric. This unique functionality, combined with their high porosity and large specific surface area, makes them highly promising for a broad range of applications [4–6]. For example, in environmental remediation, their low density and exceptional absorption capabilities make SMFs ideal candidates for efficient oil spill cleanup [7]. Similarly, their potential as high-performance thermal insulation materials is of great significance in both residential and industrial settings, where energy-efficient solutions are essential for reducing heating and cooling costs [8,9].

Many polymers exhibit intrinsic shape memory behavior due to their long-chain molecular structures and tunable phase transition temperatures. Consequently, they have been the subject of extensive research in the field of shape memory materials [10–12].

* Corresponding author.State Key Laboratory of Advanced Equipment and Technology for Metal Forming, Shandong University, Jinan, Shandong 250061, China.
E-mail address: guilong@sdu.edu.cn (G. Wang).
Peer review under the responsibility of Kingfa Scientific and Technological Co., Ltd.

https://doi.org/10.1016/j.aiepr.2025.08.002

Polyurethanes, for instance, have been widely used in SMF applications because their shape memory characteristics can be tailored by adjusting the chemical composition, such as the ratio of hard to soft segments and the degree of cross-linking [12]. However, the irreversible nature of these crosslinked networks often compromises the recyclability of the materials, thereby limiting their sustainability. In this regard, the concept of using polymer with single broad phase transition is promising, for instance, a broad glass transition achieved by fully miscible polymer blends [13–15]. When polymers with complementary properties are blended at the molecular level, they can form a homogeneous matrix with entangled long molecular chains. In the case of shape memory applications, one polymer component often serves as the "switch" segment, which responds to external stimuli, while the other acts as the "network" or "permanent" segment, providing the structural integrity and memory of the original shape. Thereby, the polymers remain their thermal plasticity that capable of producing ultralight foams.

Despite notable progress, several critical challenges persist in the development of high-performance SMFs. One of the primary difficulties is achieving ultralow-density foams without compromising structural integrity. Conventional chemical foaming techniques, which rely on the decomposition of blowing agents, often result in non-uniform foam structures due to premature or inconsistent gas evolution [16–18]. These defects manifest as large voids and uneven cell sizes, which undermine the mechanical strength and functional properties of the foams. As an alternative, physical foaming methods have gained considerable traction due to their environmental sustainability and high product quality. Particularly, supercritical carbon dioxide ($scCO_2$) is widely used as a blowing agent because of its high solubility in polymers, low cost, non-flammability, and environmental friendliness [19–22]. This technique has demonstrated great potential for producing foams with ultra-lightweight and uniform cell structures. A consistent microcellular structure is critical for achieving reliable thermal insulation, mechanical performance, and shape memory functionality. However, in practice, variations in cell size, shape, and distribution are common, which can lead to inconsistent material behavior. In oil absorption applications, many existing SMFs suffer from limited absorption capacity and poor recyclability, falling short of the stringent requirements for sustainable environmental remediation [23,24].

In this study, we address these challenges by synthesizing fully miscible PLA/PMMA polymer blends and employing supercritical CO_2 foaming to fabricate ultralight SMFs. The miscibility of PLA and PMMA was confirmed by molecular dynamics simulations and experimental analyses. Rheological investigations demonstrated that the incorporation of PMMA into the PLA matrix significantly enhanced the foamability of the blends, enabling the production of ultralight foams with high expansion ratios and refined microcellular structures. The homogeneous nature of the PLA/PMMA blends endowed the resulting foams with excellent shape memory behavior, characterized by large recoverable deformations and high shape recovery efficiency. Moreover, the combined hydrophobic and lipophilic properties of the foams resulted in highly efficient and sustainable oil absorption. The foams could be easily regenerated through simple mechanical squeezing, offering a practical and environmentally friendly solution for repeated oil-spill remediation. In addition, the high expansion ratio and open-cell structure contributed to the superior thermal insulation performance of the foams. Theoretical calculations and simulations further elucidated the heat transfer mechanisms within the foams, emphasizing the importance of minimizing solid-phase conduction to optimize insulation efficiency. The ultralight PLA/PMMA SMFs developed in this study represent a highly versatile material platform with great potential for diverse industrial applications. Notably, their outstanding shape memory properties position them as smart, multifunctional materials suitable for a wide range of advanced applications, including thermal insulation, environmental remediation, shock absorption, and acoustic damping.

2. Experimental section

2.1. Supercritical foaming of shape memory foams

The raw materials of PLA (Ingeo 4032D, NatureWorks, USA) and PMMA (CM207, ChiMei, Taiwan, China) were dried in a vacuum oven at 90 °C for 2 h to eliminate residual moisture. Pure PLA and PLA/PMMA blends were prepared using a micro twin-screw extruder (SJZS-10B, Ruiming, China) operated at a screw speed of 50 rpm with a processing temperature of 180 °C. The weight ratios of PLA to PMMA in the blends were 75/25 and 50/50, respectively. The extruded cylindrical strands, approximately 3 mm in diameter, were cooled to room temperature prior to foaming.

A batch foaming method was employed using a temperature-controlled high-pressure vessel. The extruded samples were placed in the sealed vessel, heated to 180 °C (above the melting temperature of the polymers), and saturated with supercritical carbon dioxide ($scCO_2$). The $scCO_2$ dissolved into the polymer melts, forming a homogeneous polymer/gas solution after a specified saturation time. In this study, a CO_2 pressure of 10 MPa was used as the saturation temperature, and the saturation time was set as 40 min. Subsequently, the vessel was cooled to the designated foaming temperature, followed by a rapid depressurization (about 51 $MPa{\cdot}s^{-1}$) to induce cell nucleation and growth. Finally, the foamed samples were quenched to room temperature to stabilize the cellular structures. The detailed mechanism of this supercritical foaming is illustrated in the supplementary materials.

2.2. Characterizations of the shape memory foams

The optical transparency of the samples was evaluated using a UV–vis–NIR spectrophotometer (Lambda 950, PerkinElmer, USA). Thermal transitions were analyzed via differential scanning calorimetry (DSC 3500, NETZSCH, Germany) with a heating rate of 10 °C/min from 20 °C to 200 °C under nitrogen atmosphere. Dynamic mechanical properties were assessed with a dynamic thermo-mechanical analyzer (DMA, Discovery DMA-850, TA Instruments, USA). Samples were heated from room temperature to 200 °C at 3 °C/min, under a constant frequency of 1 Hz and a preload force of 0.01 N. Fourier transform infrared spectroscopy (FTIR) spectroscopy was carried out using Nicolet 6700/NXR spectrometer (Thermo Fisher) under ATR module. The wavenumber length was from 4000 cm^{-1} to 400 cm^{-1}, with resolution of 4 cm^{-1}. Creep-recovery tests were also performed using the DMA, where samples were stretched at 80 °C under a fixed stress of 100 kPa for 2 min, followed by free recovery recording for another 2 min. Rheological properties were characterized using a rotational rheometer (Mars 40, Haake, Germany) with parallel plate geometry (diameter: 20 mm; gap: 1.2 mm) under nitrogen atmosphere. Dynamic frequency sweep tests were conducted at 180 °C with a strain amplitude of 5 %, across an angular frequency range from 0.1 to 100 rad/s. The complex dielectric permittivity ($\varepsilon^* = \varepsilon' - i\varepsilon''$) was measured using an LCR meter (E4980A, Agilent, USA) over a frequency range of 10^6 to 10^2 Hz at 80 °C with an applied AC voltage of 0.5 V. The densities of solid (ρ_s) and foam (ρ_f) samples were determined via the water displacement method. The

expansion ratio (ϕ) of the foams was calculated using the equation:

$$\phi = \frac{\rho_s}{\rho_f} \tag{3}$$

The microcellular structures of the foams were observed using a scanning electron microscope (SEM, JSM-7800F, JEOL, Japan). Prior to imaging, the foams were cut with a sharp blade and sputter-coated with a thin layer of platinum. Quantitative cellular parameters including cell size and cell density were analyzed using ImagePy software. Cell density (N_0) was calculated according to:

$$N_c = \phi\left(\frac{n}{A}\right)^{\frac{3}{2}} \tag{4}$$

where n is the number of cells in the SEM image, A is the imaged area (mm^2). The open-cell content (oc%) was measured using a nitrogen pycnometer (AccuPyc II 1340, Micromeritics, USA), according to the following equation:

$$oc\% = \frac{V_{open}}{V_{total}} = 1 - \frac{V_{true}}{V_{total}} \tag{5}$$

where V_{open}, V_{true}, and V_{total} represent the open-cell volume, true volume (including closed cells and cell walls), and total volume of the foams, respectively. Compressive properties and shape memory behavior were evaluated using a universal testing machine (HDW-2000, Hengxu, China) equipped with a heating system (Supplementary Section S1). Wettability was characterized by measuring the contact angles of deionized water and cyclohexane droplets (5 μL each) on the foam cross-sections using a contact angle analyzer (JC2000D, Powereach, China). Oil absorption performance testing were conducted by soaking the foam into oil and test their recycle absorption capacity (Supplementary Section S2). Thermal insulation performance was evaluated through both experimental measurements and theoretical calculations. The experimental thermal conductivity of foams was measured by a TPS 2500 S thermal constant tester, and further details about the calculation and simulation are provided in supplementary Section S3.

3. Results and discussion

3.1. Fully miscibility of polymer blends

As illustrated in Fig. 1a, blends of PLA and PMMA were readily prepared using a twin-screw extrusion process. During extrusion, the applied shear force promotes a high degree of miscibility between PLA and PMMA. The complete miscibility of PLA and PMMA is attributed to their similar molecular polarity, which enables strong intermolecular interactions and enhanced compatibility. This was verified using the Blends Module in Material Studio software. Fig. 1b shows the lowest-energy conformational trajectories of methyl methacrylate monomers surrounding lactic acid monomers, based on van der Waals energy minimization. The monomers are uniformly distributed on both sides of the PLA chains. The corresponding binding energy distributions are presented in Fig. 1c, where PLA-PLA, PLA-PMMA, and PMMA-PMMA interactions exhibit similar binding energies, suggesting highly compatible blending structures [25]. Fig. 1d presents the temperature dependence of the Flory-Huggins interaction parameter (χ). At the processing temperature of 200 °C, the χ value approaches zero, further confirming the excellent miscibility of PLA and PMMA [26]. This high miscibility is also demonstrated in the experimentally prepared blends. As shown in Fig. 1e, PLA/PMMA blend wafers with varying weight ratios display high optical transparency at a thickness of 2 mm. According to the transmittance spectra in Fig. 1f, all blends exhibit over 80 % transmittance in the visible wavelength range, with a slight increase in transmittance at higher PMMA contents. This increase may be due to the suppression of PLA crystallization, as evidenced by the differential scanning calorimetry (DSC) heating scans in Fig. 1g and wide-angle X-ray diffraction in Supplementary Fig. S1. Pure PLA exhibits a glass transition temperature (T_g) at 60 °C, followed by a distinct cold crystallization exothermic peak and a melting endothermic peak, reflecting its inherent crystallization behavior. In contrast, the PLA/PMMA blends display a single T_g without any separate transitions, which also confirm their complete miscibility. As the PMMA content increases, the T_g shifts to higher temperatures, and both crystallization and melting peaks disappear, due to the rigid molecular chains of PMMA inhibiting PLA crystallization [27]. Furthermore, the thermomechanical behavior was evaluated by analyzing the evolution of the damping factor (tan δ), as shown in Fig. 1h. Pure PLA exhibits a sharp and narrow tan δ peak, indicating high chain mobility and a distinct glass transition. In PLA/PMMA blends, the presence of a single tan δ peak further confirms their miscibility [28]. As PMMA content increases, the tan δ peak shifts to higher temperatures with broadened and decreased peak, indicating that molecular mobility (α-relaxation) is significantly reduced in the miscible PLA/PMMA blends. From the FTIR spectra in Supplementary Fig. S2, a new peak at 842 cm^{-1} emerges, resulting from altered C–O bond vibrational frequencies induced by hydrogen bonding between PLA's ester C–O groups and PMMA's –OH. Additionally, the shift of PLA's C═O peak from 1750 cm^{-1} to 1730 cm^{-1} indicates weakened C═O bonds due to hydrogen bonding. These observations confirm strong intermolecular interactions between PLA and PMMA. Furthermore, SEM images of the blends in Supplementary Fig. S3 reveal no second phase on the fracture surface, reinforcing the complete miscibility of the two polymers.

3.2. Foamability and cellular microstructures

Supercritical foaming technology was employed to fabricate microcellular polymer foams. However, PLA typically exhibits poor foamability due to its low melt strength, making it difficult to produce lightweight PLA foams with ultralow densities [29]. In contrast, PMMA demonstrates excellent foaming properties due to its adequate melt viscoelasticity. Therefore, introducing highly miscible PMMA molecular chains into the PLA matrix is expected to significantly enhance the foamability of the blends, enabling the production of super lightweight polymer foams. To investigate this hypothesis, the melt properties of the PLA/PMMA blends were first characterized using rotational shear rheology. As shown in Fig. 2a and b, and Supplementary Fig. S4, the PLA/PMMA blends exhibit typical viscoelastic responses, where both the storage modulus (G') and loss modulus (G'') increase with frequency. This behavior reflects restricted polymer chain mobility, resulting in a transition from viscous flow to more elastic, solid-like behavior. Notably, a significant increase in both G' and G'' with higher PMMA content implies an enhanced ability to store elastic energy and increased internal energy dissipation. This is attributed to stronger intermolecular interactions and reduced molecular mobility imparted by the rigid PMMA chains. Furthermore, the blends display Newtonian behavior at low frequencies, where the complex viscosity (η^*) remains nearly constant. As frequency increases, η^* decreases, demonstrating typical shear-thinning behavior. The presence of higher PMMA content results in significantly higher η^* values at low frequencies due to the rigidity of PMMA chains. Additionally, a

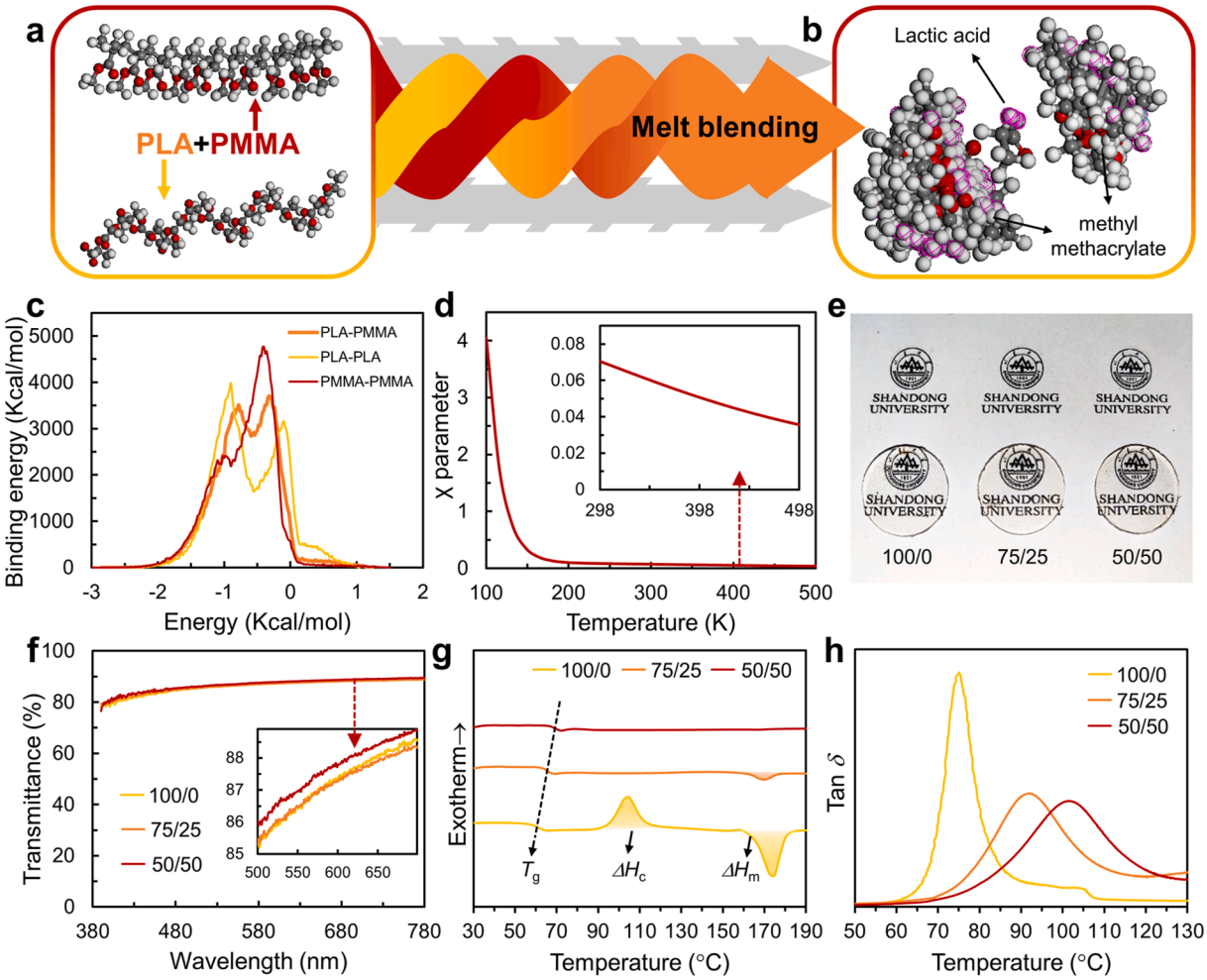

Fig. 1. Fully miscibility of the PLA/PMMA blends. (a) Molecular structures of PLA and PMMA. (b) Lowest-energy conformational trajectories of methyl methacrylate monomers surrounding lactic acid monomers, based on van der Waals energy minimization. (c) Binding energy distributions for PLA-PLA, PLA-PMMA, and PMMA-PMMA interactions. (d) Temperature dependence of the Flory-Huggins interaction parameter (χ) at 200 °C. (e) Optical photograph shows the high transparency of PLA/PMMA blend wafers with various weight ratios. (f) Light transmittance spectra of PLA/PMMA blends, exhibiting over 80 % transmittance across the visible wavelength range. (g) DSC thermograms from the first heating scan. (h) Dynamic thermomechanical analysis (DMA) of PLA/PMMA blends, illustrating variations in the damping factor (tan δ) as a function of temperature.

more pronounced shear-thinning behavior is observed at higher frequencies, arising from molecular chain alignment under shear, which reduces viscosity.

A Cole-Cole plot was used to further analyze the viscoelastic properties of the miscible blend melts (Fig. 2c). All PLA/PMMA blends exhibit single semicircular curves, indicating a single relaxation time characteristic of homogeneously miscible systems. The regular relationship between energy storage and dissipation provides further evidence of complete miscibility [30]. Moreover, the semicircle diameter increases with PMMA content, suggesting greater molecular complexity and a broader distribution of relaxation times. This phenomenon results from differences in chain relaxation dynamics and molecular weight between PLA and PMMA. The rigid PMMA chains introduce more molecular entanglements, requiring longer relaxation times and leading to a broader relaxation time distribution. In such cases, the center of the Cole-Cole plot may shift below the imaginary axis, reflecting a wide distribution in the conformations and movements of the glassy PLA/PMMA molecules.

To prepare ultralight polymer foams, batch foaming experiments were conducted in a temperature-controlled high-pressure vessel using supercritical carbon dioxide ($scCO_2$) as the blowing agent (Fig. 2d). As illustrated in Fig. 2e, a melt foaming strategy was applied, enabling the production of polymer foams with exceptionally low density and tunable cellular microstructures. This method ensures uniform polymer/gas systems Supplementary Fig. S5 while preventing adverse crystallization during foaming [31], thereby yielding high-quality PLA/PMMA foams with ultralow densities (Fig. 2f, as low as 0.0295 g/cm^3). Fig. 3a presents the volume expansion ratios of PLA/PMMA blends obtained through melt foaming. Here, the “foaming temperature window” is defined as the temperature range in which the foam expansion ratio exceeds 15. The results indicate that the width of this window increases significantly with PMMA content: from ~15 °C for pure PLA to ~27 °C and ~35 °C for blends with 25 wt % and 50 wt% PMMA, respectively. Additionally, the maximum expansion ratio (ϕ_{max}) improves markedly. Pure PLA achieves an ϕ_{max} of 31 at a foaming temperature ($T_{foaming}$) of 115 °C, whereas PLA/PMMA blends exhibit higher ϕ_{max} values of approximately 44 at elevated $T_{foaming}$ (120 °C for 25 wt% PMMA and 130 °C for 50 wt% PMMA). This corresponds to a 28.7 % further reduction in foam density. The superior foamability of PLA/PMMA blends is primarily attributed to the increased melt strength provided by PMMA, as confirmed by rheological analysis. Enhanced melt

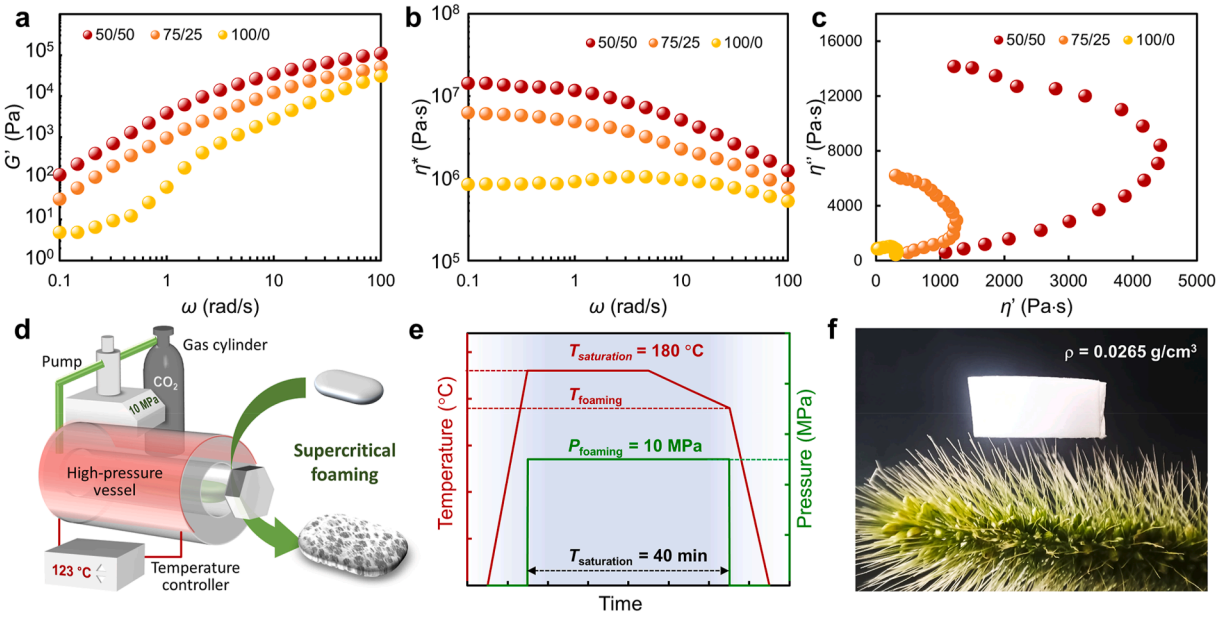

Fig. 2. Rheological properties and foaming process of the polymers. (a) Storage modulus (G'), (b) complex viscosity (η^*), and (c) Cole-Cole plots. (d) Experimental setup of the batch foaming strategy used in this study, (e) Temperature and pressure profile of the foaming process, (f) Digital photo of as-prepared PLA/PMMA (50/50) foam with ultralow density.

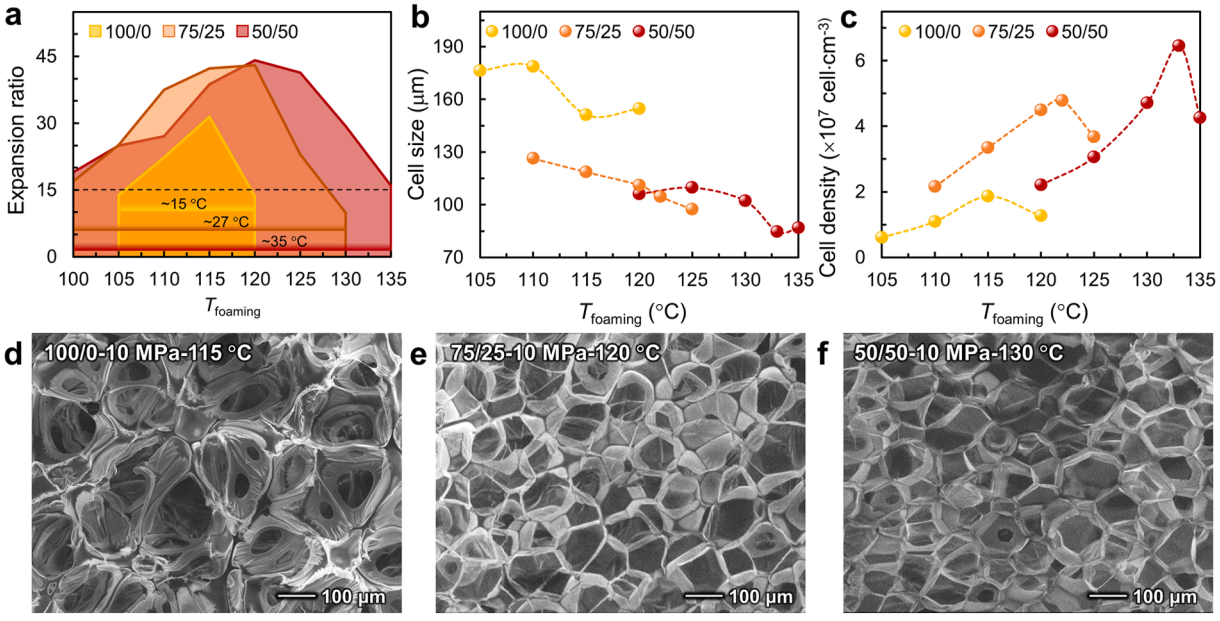

Fig. 3. Foamability and cellular structure characterization of PLA/PMMA blends with varying weight ratios. (a) Expansion ratios of foams as a function of foaming temperature. (b) Average cell sizes of foams at the optimal foaming temperature ($T_{foaming}$). (c) Cell density variations corresponding to different $T_{foaming}$. (d–f) Representative SEM images showing cellular morphology of foams at their highest expansion ratio, illustrating the effect of PMMA content on cell uniformity and structure.

strength supports cell growth and minimizes cell collapse and coalescence as the polymer melt undergoes biaxial extensional stress during foaming. Quantitative measurements of cell size and cell density (Fig. 3b and c) further support these findings. Compared to pure PLA foams, PLA/PMMA blends exhibit smaller average cell sizes and higher cell densities, owing to a reduced degree of cell coalescence. SEM images (Fig. 3d–f) of the foam morphologies at ϕ_{max} further highlight the improved foamability of the PLA/PMMA blends. While pure PLA foams display ruptured and uneven cells (Fig. 3d), the PLA/PMMA foams demonstrate finer, more uniform cellular structures with thinner cell walls (Fig. 3e and f). More SEM images of PLA/PMMA foam with different weight ratio and $T_{foaming}$ are supplied in Supplementary Figs. S6 and S7. The incorporation of PMMA significantly enhances foamability by increasing the chain rigidity of the system, as evidenced by temperature-dependent rheological data (Supplementary Fig. S8) showing a higher G', G'', and tan δ. A higher G' improves the melt's elastic recovery, enabling it to withstand internal pressure from bubble expansion during foaming, thus reducing cell wall rupture. Additionally, a lower tan δ indicates reduced

viscous dissipation, allowing the elasticity-dominated melt to maintain bubble morphology and suppress cell coalescence. This optimization of rheological properties, driven by enhanced chain rigidity, directly contributes to improved foam stability. Furthermore, uniformly dispersed PMMA microdomains act as numerous homogeneous nucleation sites, lowering the energy barrier for bubble nucleation. This promotes uniform cell nucleation and growth, minimizing variations in bubble size and enhancing overall foam uniformity.

Given the excellent foamability of the PLA/PMMA blend with a weight ratio of 50/50, further investigations into its cellular structures were conducted. Fig. 4a–c presents SEM images of PLA/PMMA foams prepared at three different foaming temperatures (125 °C, 130 °C, and 133 °C). Although these foams possess similar expansion ratios (39, 44, and 41 that corresponding to porosities of ~97.4 %, ~97.7 %, and ~97.6 % respectively), their cellular morphologies vary. At lower $T_{foaming}$ (125 °C), the foam primarily exhibits a closed-cell structure (Fig. 4a). In contrast, at higher $T_{foaming}$ (130 °C and 133 °C), an open-cell structure becomes more prominent (Fig. 4b and c). This trend is quantitatively confirmed by measuring the open-cell content (oc%) as a function of $T_{foaming}$ (Fig. 4d). The oc% increases significantly from 13.3 % to over 93.1 % as the foaming temperature rises from 120 °C to 135 °C. The increase in open-cell content is attributed to the reduced melt strength and viscosity of PLA/PMMA blends at higher temperatures, making cell walls more susceptible to rupture during expansion and promoting the interconnection of adjacent cells.

Cellular structures strongly influence the mechanical properties of foams. To investigate the load bearing property, three foams with similar expansion ratios (39, 44, and 41) but different open-cell contents were selected for compression testing. These samples were labeled as x-y oc%, where x indicates the expansion ratio and y denotes the open-cell content. As shown in Fig. 4e, the compressive stress-strain curves under 60 % single compression reveal distinct mechanical behavior. The foam 39-18 oc% exhibits a compressive strength of 0.13 MPa and an elastic modulus of 2.4 MPa. In comparison, foams 44-50 oc% and 41-88 oc% display lower compressive strengths (0.079 MPa and 0.067 MPa) and elastic moduli (1.5 MPa and 1.1 MPa), respectively (Fig. 4f). These results clearly demonstrate that increasing open-cell content leads to a decline in compressive strength and elastic modulus. Additionally, recovery performance deteriorates with higher open-cell content. This is consistent with the general understanding that closed-cell foams possess superior mechanical properties compared to open-cell foams. In open-cell structures, broken cell walls leave only thin struts to bear mechanical loads, and the absence of enclosed gas reduces both load-bearing capacity and recovery resilience. Besides, it is observed that the compressive strength and modulus increase with lower expansion ratio (Supplementary Fig. S9).

3.3. Evaluation of shape memory behaviors

Fully miscible polymer blends of PLA and PMMA have previously been reported to exhibit superior shape memory characteristics, primarily due to their broad glass transition temperature (T_g) range [28,32]. In this study, the shape memory effect of PLA/PMMA blends was first verified through a creep-recovery test. Specimens were subjected to a constant external stress of 100 kPa at 80 °C for 120 s, followed by unloading and spontaneous recovery for an additional period. Throughout this process, the strain evolution of each specimen was recorded, as shown in Fig. 5a. Pure PLA exhibited larger deformation during the creep stage and recovered only about 56 % of its initial deformation after unloading. In contrast, increasing the PMMA content resulted in reduced deformation during the creep phase and significantly improved the recovery ratio. This demonstrates that the presence of PMMA enhances both deformation resistance and shape recovery capability in the blends. When the temperature exceeds the T_g of PLA, the PLA chains can deform under external stress through the stretching and rotation of molecular bonds. This deformation

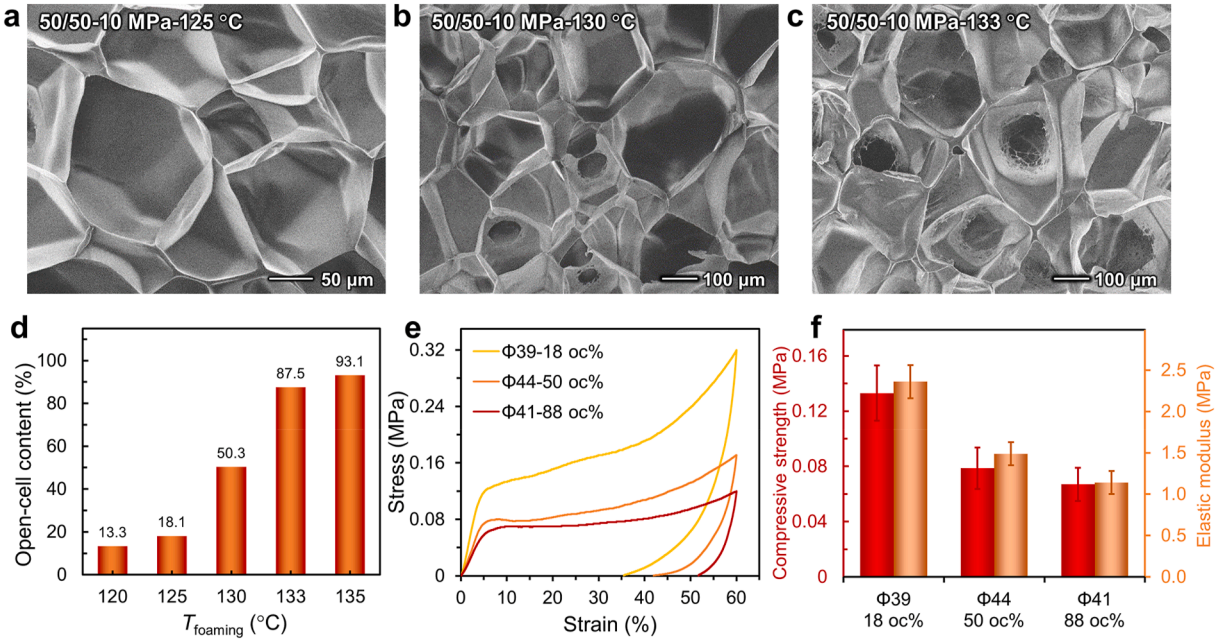

Fig. 4. Tailoring cellular morphology and mechanical properties of PLA/PMMA (50/50 wt%) foams by adjusting foaming temperature. (a–c) SEM images of foams prepared at different $T_{foaming}$. (d) Open-cell content as a function of $T_{foaming}$, highlighting the transition from closed-cell to open-cell structures with increasing temperature. (e) Compressive stress-strain curves of foams with similar expansion ratios but different open-cell content. (f) Compressive strength and elastic modulus of the corresponding foams.

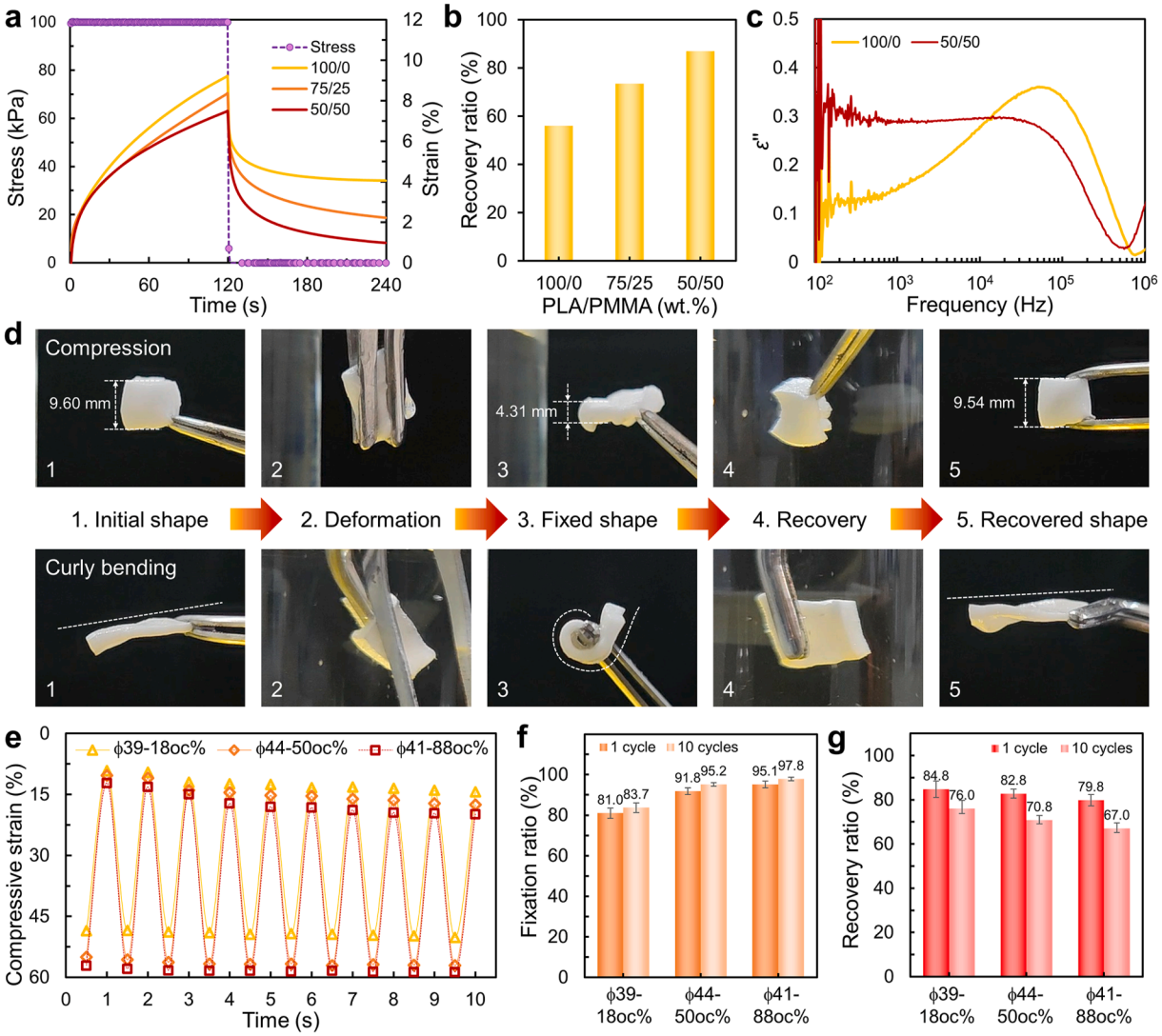

Fig. 5. Shape memory characteristics of PLA/PMMA foams. (a) Creep-recovery curves of solid PLA/PMMA blends under 100 kPa at 80 °C. (b) Creep-recovery ratio of PLA/PMMA blends with varying PMMA content. (c) Dielectric loss (ε'') spectra of solid PLA/PMMA films at 80 °C, highlighting relaxation behaviors related to the glass transition. (d) Demonstration of the shape memory effect in PLA/PMMA foams, including compressive deformation and curly bending recovery (see also supplementary Video S1). (e) Variation in compressive strain during ten compression-recovery cycles for foams with similar expansion ratio but different oc%. (f) Shape fixation ratio and (g) shape recovery ratio of the first and tenth compression-recovery cycles.

reduces entropy and imparts entropy elasticity to the molecular chains, contributing to PLA's inherent shape memory capability, where the PLA chains serve as deformable “soft domains”. The incorporation of miscible PMMA chains into the blends significantly enhances chain entanglements due to their complete miscibility. Additionally, the PMMA chains, with their higher T_g, act as “hard domains” within the network, as shown in Supplementary Fig. S10, stabilizing the permanent shape. The shape memory mechanism is further supported by the relaxation behavior of the blends in the glass transition region. The shape memory mechanism can also be verified by the relaxation behavior of the blends within the glass transition region. From the investigation through dielectric loss spectroscopy at 80 °C, as illustrated in Fig. 5c, pure PLA exhibited a dielectric loss peak at frequencies of 10^4–10^5 Hz, consistent with previous reports [28]. In comparison, the PLA/PMMA blend exhibited a broadened dielectric loss at lower frequencies, indicating increased α-relaxation heterogeneity due to the distinct dynamics of the two polymer chains [33].

Based on their excellent creep-recovery performance, PLA/PMMA foams with a 50/50 wt ratio were fabricated, which exhibited outstanding shape memory properties. As demonstrated in Fig. 5d and supplementary Video S1, one of the key advantages of SMFs is their ability to undergo both bending and compressive deformation. The shape memory effect was demonstrated in two steps: shape fixation and shape recovery. During shape fixation, the specimen was first heated to the deformation temperature (T_{deform}) and deformed under an external load. The deformed shape was then fixed by cooling to room temperature. In the shape recovery step, the specimen was reheated to T_{deform}, allowing it to recover its original shape spontaneously.

Supplementary video related to this article can be found at https://doi.org/10.1016/j.aiepr.2025.08.002

In this study, compressive-recovery tests were conducted to evaluate the strain at the fixed and recovered shapes. Ten-cycle tests were also performed to assess the durability of the shape memory effect, as shown in Fig. 5e. The corresponding shape fixation and shape recovery ratios from the first and tenth cycles are

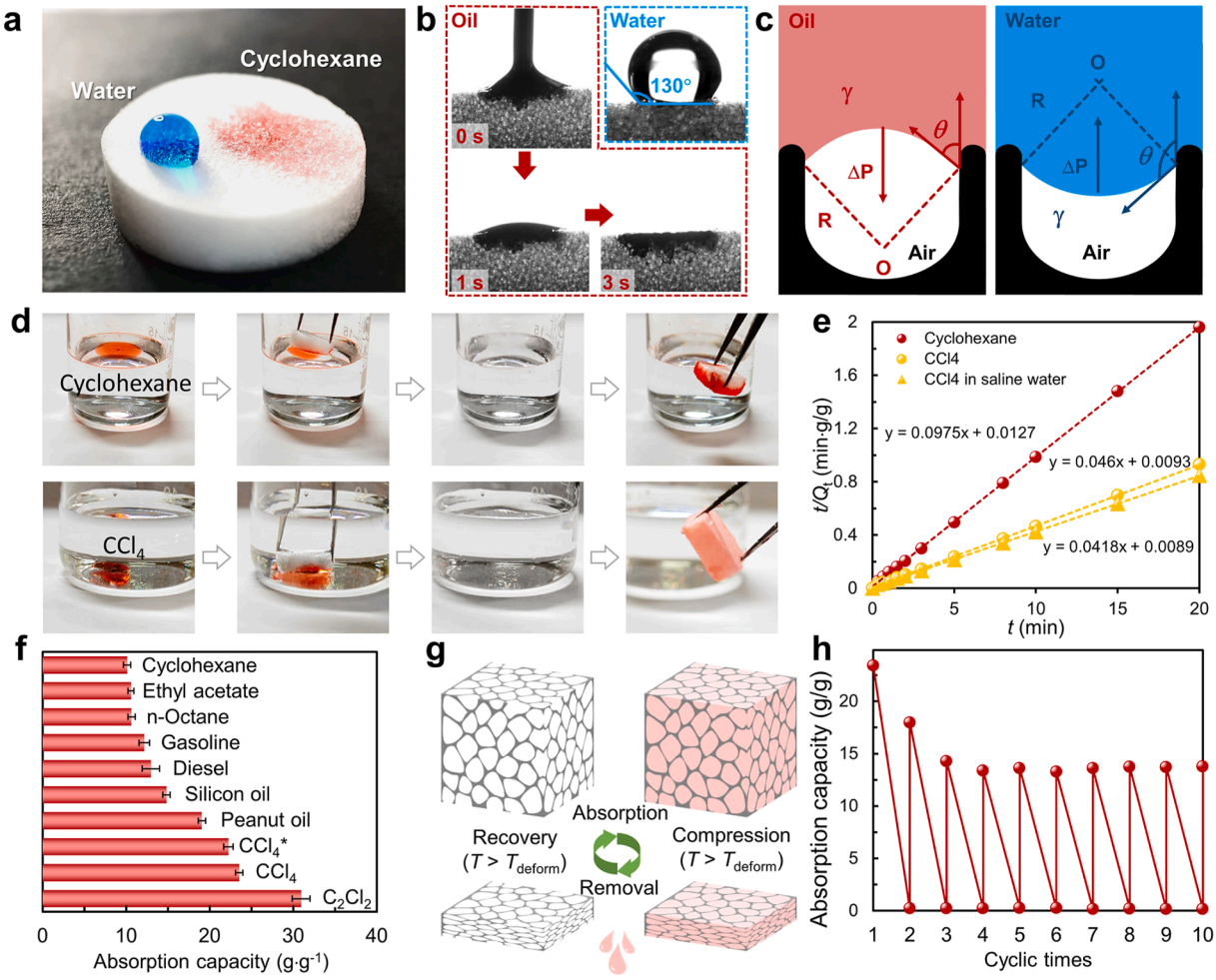

Fig. 6. Sustainable oil absorption and recovery performance of PLA/PMMA open-cell foams. (a) Photographs showing water and cyclohexane droplets on the foam surface with distinct wettability. (b) Contact angle measurements of water (~130°) and oil (~0°), demonstrating hydrophobicity and lipophilicity. (c) Schematic illustration of the oil/water selective absorption mechanism based on surface energy and pore structure (Wenzel and Cassie-Baxter states). (d) Selective removal of dyed cyclohexane (floating oil) and CCl_4 (submerged oil) from water by PLA/PMMA foams. (e) Adsorption kinetics for cyclohexane and CCl_4, fitted with a pseudo-second-order kinetic model. (f) Absorption capacities of the foams for various oils, including low- and high-viscosity types, CCl_4* indicating the oil in saline water. (g) Schematic diagram of the sustainable oil absorption and recovery process enabled by the shape memory effect. (h) Variation in oil absorption capacity during ten cyclic absorption-recovery tests.

summarized in Fig. 5f and g, respectively. To further explore the influence of foam microstructure on shape memory behavior, foams with varying open-cell contents (39-18 oc%, 44-50 oc%, and 41-88 oc%) were selected for testing. In the first cycle, it was observed that as the open-cell content increased from 18 % to 88 %, the shape fixation ratio improved from 81.7 % to 95.1 %. However, the shape recovery ratio decreased from 84.8 % to 79.8 %. The trade-off between shape fixation and recovery ratios with varying open-cell content is closely linked to the presence of gas trapped within microcells. At low open-cell content, where closed cells predominate, a larger amount of gas is trapped within these cells. During shape fixation, this trapped gas is readily compressed, generating internal pressure that disrupts stable deformation fixation, resulting in a lower fixation ratio. Conversely, during shape recovery, the release of this compressed gas pressure aids material rebound, leading to a higher recovery ratio. As open-cell content increases, the proportion of closed cells and trapped gas decreases. In the fixation stage, gas escapes rapidly through open cells, reducing internal pressure interference and thereby improving the fixation ratio. However, in the recovery stage, the absence of auxiliary gas pressure and increased energy dissipation in open-cell structures lead to a slight reduction in the recovery ratio. Additionally, as shown in Fig. 5e, the foam exhibits a noticeable decrease in shape recovery ratio during the first three cycles of a ten-cycle test, stabilizing in the subsequent seven cycles. The significant decline in the shape recovery ratio during the initial three cycles is likely due to structural adjustments, such as polymer chain relaxation and microstructural changes, which temporarily impair the foam's ability to return to its original shape. The stabilization observed in the following seven cycles suggests that the foam reaches a structural equilibrium, where these adjustments are complete, enabling consistent shape recovery. In conclusion, PLA/PMMA shape memory foams exhibit tunable deformation and recovery behaviors, which are influenced by their composition and microporous structure. However, there is an inherent trade-off between shape fixation and recovery performance in practical applications.

3.4. Sustainable oil absorption by shape memory foams

Polymer foams with open-cell microporous structures have been extensively applied in oil absorption due to their high porosity and surface area [23,34]. In this study, we investigated the oil absorption capabilities of PLA/PMMA open-cell foams, with a

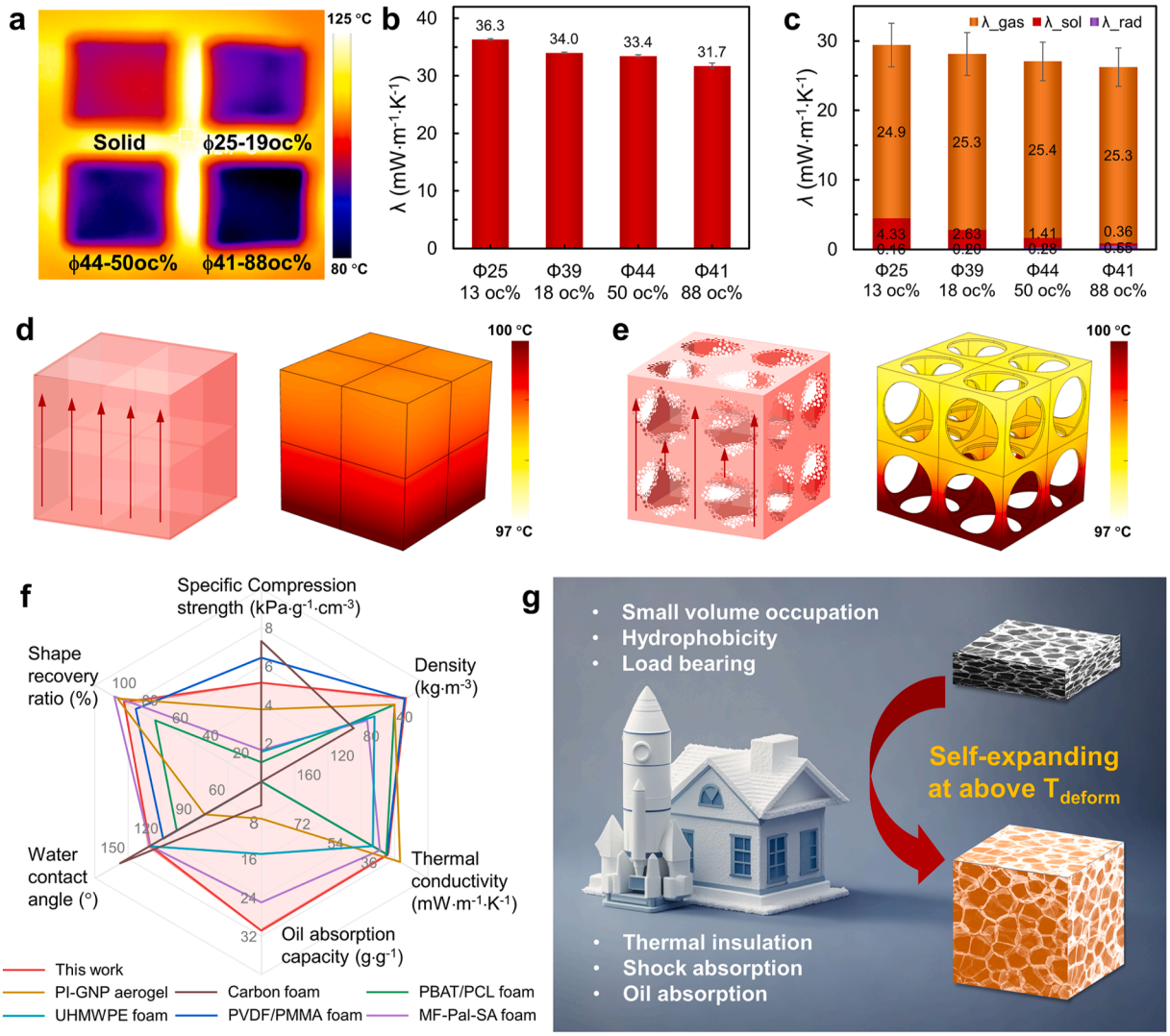

Fig. 7. Thermal insulation and comprehensive properties of the PLA/PMMA foams. (a) Infrared thermal images of solid and foam samples placed on a hot plate at 130 °C, showing differences in surface temperature. (b) Measured thermal conductivities of PLA/PMMA foams with various microcellular structures. (c) Theoretically calculated thermal conductivity components, showing the contributions from the solid, gas, and radiative parts. (d,e) Thermal conduction scheme and COMSOL simulation analysis of foams with (d) closed-cell and (e) open-cell structures. (f) Comparison of key properties of the ultralight PLA/PMMA foams with previously reported advanced porous polymer foams. (g) Schematic illustration of the shape memory effect enabling smart and reusable applications of PLA/PMMA foams.

particular focus on their sustainable recovery enabled by shape memory behavior. The wettability of water and oil on the foam surface was first characterized to assess their selectivity in oil/water separation. As shown in Fig. 6a, a water droplet maintains a spherical shape and rests on the foam surface, while a cyclohexane droplet rapidly spreads and infiltrates the pores. This behavior demonstrates the excellent hydrophobicity and lipophilicity of the open-cell foams. Contact angle measurements in Fig. 6b further confirm this phenomenon: a 5 μL droplet of cyclohexane is completely absorbed by the foam within 1 s, while an equal volume of water maintains a high contact angle of approximately 130°. Notably, it is found that a higher expansion ratio results in increased water contact angle (Supplementary Fig. S11). This distinct difference in wettability arises from the combination of the foam's microporous structure and its enhanced surface roughness. According to the Young-Laplace equation [35]:

$$\Delta P = \frac{2\gamma \cos\theta}{R} \tag{1}$$

where ΔP is the additional Laplace pressure, γ is the liquid's surface tension, θ is the contact angle, and R is the pore radius. As illustrated in Fig. 6c, an oil contact angle (θ) less than 90° results in a positive ΔP, promoting capillary-driven infiltration of oil into the pores (Wenzel state). Conversely, for water, the contact angle exceeds 90°, producing a negative ΔP, which prevents water penetration and retains it in a Cassie-Baxter state where water droplets remain suspended on the surface. This remarkable wettability selectivity allows the foams to efficiently absorb oil from aqueous environments. Fig. 6d and supplementary Video S2 demonstrates the removal of two types of oil (dyed red): cyclohexane floating on the water surface and carbon tetrachloride (CCl_4) sinking in water.

The foams rapidly absorb both oils, achieving efficient and selective oil collection. The adsorption capacity as a function of time for both oils is presented in Supplementary Fig. S11, indicating a rapid uptake that reaches equilibrium within 5 min. The adsorption kinetics were further analyzed using a pseudo-second-order kinetic model [36]:

$$\frac{t}{Q_t}=\frac{t}{Q_e}+\frac{1}{kQ_e^2} \quad (2)$$

where k is the adsorption rate constant, t is the adsorption time, Q_t is the adsorption capacity at time t, and Q_e is the theoretical equilibrium adsorption capacity. As shown in Fig. 6e, linear fitting of the t/Q_t data provides k values of 0.75 g g^{-1}·min^{-1} for cyclohexane and 0.20 g g^{-1}·min^{-1} for CCl_4, demonstrating competitive performance relative to previously reported polymer foams [15,20,37,38]. Additionally, the foams exhibit high absorption capacities for a wide range of oils, including viscous oils such as peanut oil and silicone oil. As presented in Fig. 6f, absorption capacities range from 10.1 to 30.9 g g^{-1}, confirming the versatility of the open-cell foams for different oil types. Additionally, we conducted supplementary experiments on oil absorption in saline water. As shown in Fig. 6e and f, and Supplementary Fig. S12, using CCl_4 in a 3.5 % NaCl solution as an example, the foam exhibits comparable but slightly reduced oil absorption capacity and kinetics in saline water compared to deionized (DI) water. This reduction may be attributed to the higher ionic content in saline water, which weakens the foam's hydrophobicity by shielding surface charges and increases surface tension.

3.5. Enhanced thermal insulation property by open-cell structure

To evaluate the thermal insulation performance of the prepared PLA/PMMA foams with different microcellular structures, we systematically investigated their thermal conductivity as a function of expansion ratio and open-cell content. As shown in Fig. 7a, the thermal insulation behavior was first assessed by placing foam samples on a hot stage maintained at 130 °C and recording their upper surface temperatures via infrared thermal imaging. All foam samples demonstrated significantly better thermal insulation compared to the solid PLA/PMMA sample, as evidenced by the lower surface temperatures. Among them, the foam with an expansion ratio of 41 and open-cell content of 88 % exhibited the best thermal insulation at a thermal conductivity as low as 31.7 mW m^{-1} K^{-1}, outperforming the samples with 25-19 oc% and 44-40 oc% expansion ratio/open-cell contents, respectively. To quantitatively confirm these observations, the effective thermal conductivity (λ_{exp}) of the foams was measured using the transient plane source (TPS) method (Fig. 7b). When comparing foams with similar open-cell content (e.g., 13 % and 18 %), it was found that a higher expansion ratio substantially decreased thermal conductivity due to the reduced solid-phase volume fraction. Conversely, at similar expansion ratios of ~40, increasing the open-cell content led to further reductions in thermal conductivity, suggesting the beneficial effect of open-cell structures on thermal insulation. To better understand the underlying mechanisms, we theoretically calculated the contributions of the solid, gas, and radiative phases to the total thermal conductivity based on the foams' microcellular structural parameters [39,40]. The calculated results (Fig. 7c) showed a consistent trend with the experimental measurements. Specifically, the contribution from the solid phase (λ_{sol}) decreased significantly with increasing expansion ratio and open-cell content, while the contributions from the gas (λ_{gas}) and radiation (λ_{rad}) phases increased slightly. These results indicate that the reduced solid-phase thermal conduction is primarily responsible for the improved thermal insulation in the foams. This is consistent with the general understanding that higher expansion ratios lead to lower foam density, reducing the proportion of the highly thermally conductive solid phase and, therefore, lowering the overall thermal conductivity. However, as foam density continues to decrease, radiative heat transfer and convective effects within the pores may become more significant and limit further improvement. Under such conditions, open-cell structures can provide additional benefits by disrupting heat transfer pathways, leading to further reductions in thermal conduction. In open-cell foams, heat transfer through the interconnected pore walls is more restricted compared to closed-cell structures, which contributes to superior thermal insulation. To visually demonstrate these effects, three-dimensional models (Fig. S13) of closed-cell and open-cell foam structures were developed and analyzed using COMSOL Multiphysics software. In Fig. 7d and e, the simulation results revealed that under the same heat source temperature of 100 °C, the open-cell foam exhibited a lower upper surface temperature than the closed-cell counterpart, indicating enhanced thermal insulation.

4. Conclusion

In summary, this study demonstrates the development of ultralight PLA/PMMA blend foams exhibiting outstanding comprehensive performance and a pronounced shape memory effect. Compared to previously reported polymer foams, the PLA/PMMA foams presented here offer superior properties, as illustrated in Fig. 7f and Table S1 [20,37,41–43]. The seamless miscibility between PLA and PMMA, driven by their comparable molecular polarity and strong intermolecular interactions, was confirmed through molecular dynamics simulations, differential scanning calorimetry (DSC), and thermomechanical analysis. The incorporation of PMMA significantly improved the foamability of the PLA matrix, as evidenced by enhanced rheological properties and the successful fabrication of ultralight foams via supercritical CO_2 foaming technology. Owing to the increased melt strength imparted by PMMA, the PLA/PMMA blends outperformed pure PLA in terms of foaming ability, achieving higher expansion ratios and lower densities. The resultant foams exhibited highly refined cellular structures, characterized by smaller cell sizes, higher cell densities, and improved uniformity, which contributed to enhanced structural integrity. In addition, the PLA/PMMA foams demonstrated excellent shape memory behavior, enabling significant deformation and rapid recovery upon thermal triggering. This shape recoverability, combined with their pronounced hydrophobicity and lipophilicity, facilitated efficient and sustainable oil absorption and recovery. The absorbed oils could be easily extracted through mechanical squeezing, allowing for multiple reuse cycles with minimal performance degradation. Moreover, the foams exhibited superior thermal insulation performance, attributed to their optimized expansion ratio and open-cell content. Both theoretical calculations and COMSOL simulations highlighted the critical role of reducing solid-phase heat transfer in achieving lower thermal conductivity.

Overall, the ultralight PLA/PMMA foams emerge as a versatile material platform with significant potential for a wide range of industrial applications. Their shape memory effect not only enhances mechanical performance but also enables smart, multifunctional functionalities across various scenarios. As illustrated in Fig. 7g, the foams can be compressed into a compact form for convenient transportation and exhibit excellent load-bearing capabilities in this state. Upon exposure to temperatures above their deformation temperature (T_{deform}), the foams can rapidly self-expand into ultralight, low-density structures, unlocking

potential applications in thermal insulation, shock absorption, and acoustic damping.

CRediT authorship contribution statement

Jialong Chai: Writing – original draft, Methodology, Investigation, Data curation, Conceptualization. **Guilong Wang:** Writing – review & editing, Supervision, Investigation, Funding acquisition. **Chao Wei:** Methodology, Investigation. **Xinyang Li:** Methodology, Investigation. **Runze Shao:** Formal analysis, Data curation. **Guoqun Zhao:** Supervision, Project administration.

Declaration of competing interest

The authors declare that they have no known competing financial interests or personal relationships that could have appeared to influence the work reported in this paper.

Acknowledgement

This work was supported National Natural Science Foundation of China (Grant No. 52175341), Shandong Provincial Natural Science Foundation (Grant No. ZR2022JQ24), Funding Project of Jinan City's New Twenty Items for Colleges and Universities (Grant No. 202333038), Excellent Young Team Project of Central Universities (Grant No. 2023QNTD002), and Qingdao Key Technology Research and Industrialization Demonstration Project (Grant No. 24-1-2-qljh-10-gx).

Appendix A. Supplementary data

Supplementary data to this article can be found online at https://doi.org/10.1016/j.aiepr.2025.08.002.

References

[1] Z. Tang, G. Deng, Y. Sun, L. Tao, C. Wang, Z. Yang, P. Liu, Q. Wang, Y. Zhang, T. Wang, 4D printing of high-performance shape memory polymer with double covalent adaptive networks, Adv. Ind. Eng. Polym. Res. (2025), https://doi.org/10.1016/j.aiepr.2024.11.002.
[2] S. Sarrafan, G. Li, Conductive and ferromagnetic syntactic foam with shape memory and self-Healing/Recycling capabilities, Adv. Funct. Mater. 34 (2024) 2308085, https://doi.org/10.1002/adfm.202308085.
[3] X. Jia, B. Shen, L. Zhang, W. Zheng, Construction of shape-memory carbon foam composites for adjustable EMI shielding under self-fixable mechanical deformation, Chem. Eng. J. 405 (2021) 126927, https://doi.org/10.1016/j.cej.2020.126927.
[4] M. Guo, Y. Zhang, C. Huang, X. Zhao, X.P. Yan, Y. Huang, L. Li, T. Liu, Shape memory polyimide aerogel composites with high programming temperatures and exceptional shape recovery capability, Compos. Part A Appl. Sci. Manuf. 174 (2023) 107717, https://doi.org/10.1016/j.compositesa.2023.107717.
[5] L. Zhang, H. Li, X. Lai, X. Su, T. Liang, X. Zeng, Thiolated graphene-based superhydrophobic sponges for oil-water separation, Chem. Eng. J. 316 (2017) 736–743, https://doi.org/10.1016/j.cej.2017.02.030.
[6] P. Xiang, H. Zhang, Q. Zhang, Z. Yu, Y. Wang, J. Li, J. Lei, Mild fabrication of polymeric porous/nonporous micro-composite structures via enhancing the photothermal conversion of ultrafast laser, Adv. Funct. Mater. 34 (2024) 2410304, https://doi.org/10.1002/adfm.202410304.
[7] M. Sehrawat, V. Singh, M. Rani, C. Kalra, S. Bharadwaj, R. Rani, A. Bisht, B. P. Singh, Nano-welded carbon nanotube sponges for efficient oil spill remediation, J. Clean. Prod. 467 (2024) 142841, https://doi.org/10.1016/j.jclepro.2024.142841.
[8] Z. Shi, G. Zhao, L. Zhang, G. Wang, J. Chai, Ultralight and hydrophobic PVDF/PMMA open-cell foams with outstanding heat-insulation and oil-adsorption performances fabricated by CO2molten foaming, J. CO2 Util. 63 (2022) 102108, https://doi.org/10.1016/j.jcou.2022.102108.
[9] J.J. Kouadjo Tchekwagep, Z. Li, H. Shifeng, J. Huang, H.K. Tchakouté, Transforming waste into sustainable insulation: a novel thermal insulation board utilizing treated rice husk ash, bagasse ash, and expanded vermiculite in calcium sulfoaluminate cement composite, J. Clean. Prod. 512 (2025), https://doi.org/10.1016/j.jclepro.2025.145699.
[10] K. Ruenpanya, P. Mora, P. Karagiannidis, K. Bunyanuwat, S. Rimdusit, Magnetic-responsive triple shape memory polymer from bio-based benzoxazine/urethane polymer alloys with iron oxide nanoparticles, Adv. Ind. Eng. Polym. Res. (2024), https://doi.org/10.1016/j.aiepr.2024.07.001.
[11] W. Liu, Y. He, J. Leng, Humidity-responsive shape memory polyurea with a high energy output based on reversible cross-linked networks, ACS Appl. Mater. Interfaces 15 (2023) 2163–2171, https://doi.org/10.1021/acsami.2c18489.
[12] T. Xie, Tunable polymer multi-shape memory effect, Nature 464 (2010) 267–270, https://doi.org/10.1038/nature08863.
[13] G. Fredi, A. Dorigato, Compatibilization of biopolymer blends: a review, Adv. Ind. Eng. Polym. Res. 7 (2024) 373–404, https://doi.org/10.1016/j.aiepr.2023.11.002.
[14] X. Hong, Y. Li, Y. Zheng, Q. Li, Constructing a biomass flame retardant for fire-safe, thermal management, and compressive strength application of polybutylene adipate terephthalate/polylactic acid foams, Adv. Ind. Eng. Polym. Res. (2025), https://doi.org/10.1016/j.aiepr.2024.12.003.
[15] J. Zhao, Y. Huang, G. Wang, Y. Qiao, Z. Chen, A. Zhang, C.B. Park, Fabrication of outstanding thermal-insulating, mechanical robust and superhydrophobic PP/CNT/sorbitol derivative nanocomposite foams for efficient oil/water separation, J. Hazard. Mater. 418 (2021) 126295, https://doi.org/10.1016/j.jhazmat.2021.126295.
[16] L.M.M. Machado, S.F. Lütke, D. Perondi, C. Manera, M. Godinho, G.C. Collazzo, L.F.O. Silva, T.J. Crissien, N. Ahmad, S. Mohandoss, G.L. Dotto, Journal of environmental chemical engineering Eco-friendly foams from eucalyptus-bleached cellulose biochars for organic contaminant adsorption in oilfield water, J. Environ. Chem. Eng. 13 (2025) 115652, https://doi.org/10.1016/j.jece.2025.115652.
[17] Y. Tian, X. Feng, C. Wang, S. Shang, H. Liu, X. Huang, J. Jiang, Z. Song, H. Zhang, Fully biobased degradable vitrimer foams: mechanical robust, catalyst-free self-healing, and shape memory properties, ACS Appl. Mater. Interfaces 16 (2024) 6523–6532, https://doi.org/10.1021/acsami.4c00267.
[18] G. Wang, G. Wan, J. Chai, B. Li, G. Zhao, Y. Mu, C.B. Park, Structure-tunable thermoplastic polyurethane foams fabricated by supercritical carbon dioxide foaming and their compressive mechanical properties, J. Supercrit. Fluids 149 (2019) 127–137, https://doi.org/10.1016/j.supflu.2019.04.004.
[19] X. Sun, G. Wang, Z. Xu, J. Chai, A. Zhang, G. Zhao, S. Li, Y. Wang, H. Jiao, Microcellular foaming-derived strong ultra-high molecular weight polyethylene/high-density polyethylene foams for thermally insulating and oil-water separating applications, J. Environ. Chem. Eng. 12 (2024) 113992, https://doi.org/10.1016/j.jece.2024.113992.
[20] J. Wang, J. Chai, G. Wang, J. Zhao, D. Zhang, B. Li, H. Zhao, G. Zhao, Strong and thermally insulating polylactic acid/glass fiber composite foam fabricated by supercritical carbon dioxide foaming, Int. J. Biol. Macromol. 138 (2019) 144–155, https://doi.org/10.1016/j.ijbiomac.2019.07.071.
[21] J. Chai, G. Wang, A. Zhang, G. Dong, S. Li, J. Zhao, G. Zhao, Microcellular injection molded lightweight and tough poly (L-lactic acid)/in-situ polytetrafluoroethylene nanocomposite foams with enhanced surface quality and thermally-insulating performance, Int. J. Biol. Macromol. 215 (2022) 57–66, https://doi.org/10.1016/j.ijbiomac.2022.06.091.
[22] O. King, E. Constant, A.C. Weems, Shape memory Poly(β-hydroxythioether) foams for oil remediation in aquatic environments, ACS Appl. Mater. Interfaces 13 (2021) 20641–20652, https://doi.org/10.1021/acsami.1c02630.
[23] Z. Cheng, P. Liu, H. Lai, X. Luo, Q. Xia, D. Zhang, Y. Liu, L. Jiang, Superlyophilic shape memory porous sponge for smart liquid permeation, ACS Nano 14 (2020) 14047–14056, https://doi.org/10.1021/acsnano.0c06673.
[24] G.K. Zhao, F.Z. Li, E.L. Cui, M.Q. Zhu, Binary blends of Eucommia ulmoides gum and nitrile butadiene rubber based on materials studio: compatibility prediction, preparation and properties characterization, Ind. Crops Prod. 204 (2023) 117255, https://doi.org/10.1016/j.indcrop.2023.117255.
[25] S. Antoine, Z. Geng, E.S. Zofchak, M. Chwatko, G.H. Fredrickson, V. Ganesan, C. J. Hawker, N.A. Lynd, R.A. Segalman, Non-intuitive trends in flory-huggins interaction parameters in polyether-based polymers, Macromolecules 54 (2021) 6670–6677, https://doi.org/10.1021/acs.macromol.1c00134.
[26] X. Hao, J. Kaschta, X. Liu, Y. Pan, D.W. Schubert, Entanglement network formed in miscible PLA/PMMA blends and its role in rheological and thermo-mechanical properties of the blends, Polymer (Guildf). 80 (2015) 38–45, https://doi.org/10.1016/j.polymer.2015.10.037.
[27] C. Samuel, S. Barrau, J.M. Lefebvre, J. Raquez, P. Dubois, Designing multiple-shape memory polymers with miscible polymer blends: evidence and origins of a triple-shape memory effect for miscible PLLA/PMMA blends, Macromolecules 47 (2014) 6791–6803, https://doi.org/10.1021/ma500846x.
[28] J. Chai, G. Wang, J. Zhao, A. Zhang, Z. Shi, C. Wei, Microcellular PLA/PMMA foam fabricated by CO 2 foaming with outstanding shape-memory performance, J. CO2 Util. 49 (2021) 101553, https://doi.org/10.1016/j.jcou.2021.101553.
[29] K. Li, J. Peng, L.-S. Turng, H.-X. Huang, Dynamic rheological behavior and morphology of polylactide/poly(butylenes adipate-co-terephthalate) blends with various composition ratios, Adv. Polym. Technol. 30 (2011) 150–157, https://doi.org/10.1002/adv.
[30] J. Hou, G. Zhao, G. Wang, L. Zhang, G. Dong, B. Li, Ultra-high expansion linear polypropylene foams prepared in a semi-molten state under supercritical CO2, J. Supercrit. Fluids 145 (2019) 140–150, https://doi.org/10.1016/j.supflu.2018.11.017.
[31] F.J. Eshkaftaki, I. Ghasemi, Multiple-shape memory behavior of nanocomposite based on polymethylmethacrylate/poly (lactic acid)/graphene

nanoplatelets (PMMA/PLA/GNP), Polym. Bull. 75 (2018) 4073–4084, https://doi.org/10.1007/s00289-017-2252-3.
[32] X. Ji, D. Chen, Y. Zheng, J. Shen, S. Guo, E. Harkin-Jones, Multilayered assembly of poly(vinylidene fluoride) and poly(methyl methacrylate) for achieving multi-shape memory effects, Chem. Eng. J. 362 (2019) 190–198, https://doi.org/10.1016/j.cej.2019.01.016.
[33] X. Chen, Y.N. Liang, X.Z. Tang, W. Shen, X. Hu, Additive-free poly (vinylidene fluoride) aerogel for oil/water separation and rapid oil absorption, Chem. Eng. J. 308 (2017) 18–26, https://doi.org/10.1016/j.cej.2016.09.038.
[34] S. Shi, Y. Tang, G. Wang, J. Zhao, G. Wan, L. Wu, J. Wang, C.B. Park, G. Wang, Tailoring surface features and pore structure by carbon spiral fibers to construct the high-strength carbon foams for the fast and cyclic photothermal oil absorption, J. Mater. Sci. Technol. 150 (2023) 190–200, https://doi.org/10.1016/j.jmst.2022.12.019.
[35] B. Li, G. Zhao, G. Wang, L. Zhang, J. Gong, Z. Shi, Biodegradable PLA/PBS open-cell foam fabricated by supercritical CO2 foaming for selective oil-adsorption, Sep. Purif. Technol. 257 (2021) 117949, https://doi.org/10.1016/j.seppur.2020.117949.
[36] Z. Wang, G. Wang, Z. Xu, A. Zhang, G. Zhao, Poly(caprolactone) enabled ultralight and recyclable poly(butylene adipate-co-terephthalate) foams for thermal insulation application, ACS Sustain. Chem. Eng. 12 (2024) 13231–13243, https://doi.org/10.1021/acssuschemeng.4c04345.
[37] M. Chhajed, C. Verma, P. Gupta, P.K. Maji, Multifunctional esterified nanocellulose aerogel: impact of fatty chain length on oil/water separation and thermal insulation, Cellulose 30 (2023) 1717–1739, https://doi.org/10.1007/s10570-022-04993-w.
[38] J. Torre, V. Bernardo, J. Pinto, M.Á. Rodríguez-Pérez, Contribution of the radiative transfer mechanism to the total thermal conductivity of anisotropic porous materials, Polym. Test. 136 (2024) 108487, https://doi.org/10.1016/j.polymertesting.2024.108487.
[39] V. Bernardo, J. Martin-de Leon, J. Pinto, R. Verdejo, M.A. Rodriguez-Perez, Modeling the heat transfer by conduction of nanocellular polymers with bimodal cellular structures, Polymer (Guildf). 160 (2019) 126–137, https://doi.org/10.1016/j.polymer.2018.11.047.
[40] O.A. Tafreshi, S. Ghaffari-Mosanenzadeh, Z. Ben Rejeb, Z. Saadatnia, M. M. Rastegardoost, C. Zhang, C.B. Park, H.E. Naguib, Amphiphilic polyimide-graphene nanoplatelet aerogel composites with high mechanical stability and enhanced thermal insulation properties for oil sorption applications, Mater. Today Sustain. 22 (2023) 100403, https://doi.org/10.1016/j.mtsust.2023.100403.
[41] S. Wu, D. Chen, G. Zhao, Y. Cheng, B. Sun, X. Yan, W. Han, G. Chen, X. Zhang, Controllable synthesis of a robust sucrose-derived bio-carbon foam with 3D hierarchical porous structure for thermal insulation, flame retardancy and oil absorption, Chem. Eng. J. 434 (2022) 134514, https://doi.org/10.1016/j.cej.2022.134514.
[42] Z. Shi, G. Zhao, G. Wang, L. Zhang, C. Wei, J. Chai, Development of ultralight, tough and hydrophobic polymethylmethacrylate/polyvinylidene fluoride shape memory foams for heat insulation applications, Mater. Des. 225 (2023) 111527, https://doi.org/10.1016/j.matdes.2022.111527.
[43] H. Jin, X. Zhou, Y. Gu, C. Dai, S. Yun, P. Mao, G. Guan, J. Chen, Multifunctional melamine formaldehyde composite foam for high-temperature insulation, flame retardancy, and oil-water separation, Ind. Eng. Chem. Res. 61 (2022) 6458–6467, https://doi.org/10.1021/acs.iecr.2c00245.